Time-Resolved Vector-Field Imaging of Spin-Wave Propagation in Permalloy Stripes Using Wide-Field Magneto-Optical Kerr Microscopy

Takeshi Ogasawara[*]

National Institute of Advanced Industrial Science and Technology (AIST), Tsukuba, Ibaraki 305-8565, Japan

The propagation of magnetostatic surface spin waves in permalloy stripes was observed by high-resolution wide-field magneto-optical Kerr microscopy using the stroboscope technique. A long-time stable semiconductor-laser light source was employed and uniform illumination using a fiber speckle reducer and active stabilization of the focus and the sample position were achieved. These enabled the measurement of spin waves at a frequency of 5.6 GHz in a minimum stripe width of 2 μm with a sensitivity of 1% saturation magnetization. A pronounced self-focusing effect was observed, which is explained by the peculiar dispersion relation of the spin wave. The capability of measuring all three vector components of magnetization allows direct observation of spin waves as a propagation of precessional motion.

I. INTRODUCTION

Ferromagnetic materials have played a major role in information recording. The concept of using spin not only for information recording but also for information transfer and processing has grown as the technology for controlling spin has become more sophisticated with the development of spintronics. Magnonics, which is a field of research that has developed rapidly in the past decade, utilizes spin waves for these purposes [1].

An important aspect of spin-wave research is the detection technique of spin waves, particularly for imaging spin waves in thin films. Techniques such as microfocus Brillouin scattering [2–8], scanning transmission X-ray microscopy [9–11], and time-resolved magneto-optical Kerr microscopy are frequently used for imaging spin waves [12–19]. New methods such as heterodyne detection have also been developed [20].

Microfocus Brillouin scattering is the primary method that has produced many important results in this field [2–8]. This method is essentially a frequency-domain measurement and therefore its temporal resolution is inversely proportional to its frequency resolution. The typical temporal resolution is a few nanoseconds, which is comparable to the lifetime of the spin waves in metallic magnetic thin films. Scanning transmission x-ray microscopy, which is an advanced technique that has led to many achievements in recent years, has high temporal and spatial resolution [9–11]. However, because of the requirement for synchrotron-radiation facilities, its applications are limited and it is difficult to obtain sufficient experimental time.

Time-resolved magneto-optical microscopy is another frequently used technique [12–19]. Thus far, measurements have been performed using the scanning method based on the polar Kerr effect. The polar Kerr effect can only observe the magnetization component perpendicular to the plane; however, all three components of the magnetization vector can be detected independently by combining the polar and longitudinal Kerr effects [18,21–23].

In this study, stroboscopic time-resolved magnetic imaging measurements using wide-field magneto-optical Kerr microscopy were achieved. These were enabled using a picosecond-pulsed semiconductor laser as a stable light source and by uniform illumination with a fiber speckle reducer and active stabilization of the focus and the sample position. The propagation of multigigahertz magnetostatic surface spin waves in permalloy microstructures was observed with three components of the magnetization vector, submicrometer spatial resolution, and 1% saturation magnetization sensitivity.

II. EXPERIMENTAL SETUP

The configuration of the measurement system is schematically shown in Fig. 1. It is based on a system previously reported in Refs. [23,24]. The key features of the system are a high-resolution magneto-optical Kerr microscope, a laser-diode light source, and a multimode fiber-based speckle reducer and active stabilization of the focus and the sample position.

The principle of the high-resolution magneto-optical Kerr microscope has already been described in detail in Ref. [23]; hence I will just describe it briefly here, for the convenience of the readers. In a magneto-optical Kerr
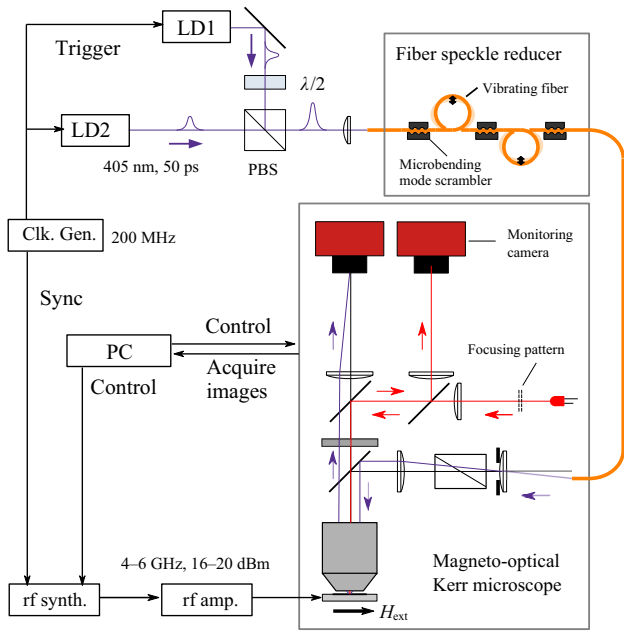
_____
[*]t-ogasawara@aist.go.jp

FIG. 1.   The configuration of the measurement system: LD, laser diode; PBS, polarizing beam splitter; rf, radio frequency.
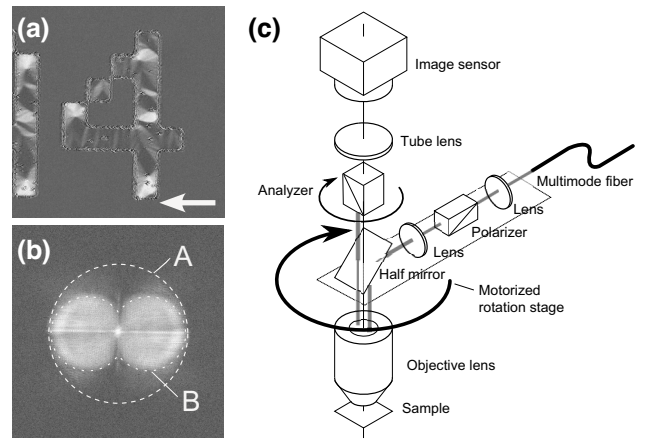

FIG. 2.   (a) An example of a domain image observed using the conventional method. The arrow indicates the direction of incidence. (b) The Fourier-transformed image of (a). The dashed circle indicates the frequency cutoff corresponding to the maximum resolution. (c) A schematic of the optical system of the high-resolution magneto-optical Kerr microscope. The illumination direction (azimuth angle) is changed by rotating the illumination path.

microscope capable of observing in-plane magnetization, it is necessary to inject illumination from the edge of the rear aperture of the objective lens in order to utilize the longitudinal magneto-optical Kerr effect. The spatial resolution is degraded under this condition. Figures 2(a) and 2(b) show an example of a magnetic domain image observed by a conventional method and its Fourier-transformed image, respectively. The illumination is incident from the direction of the arrow to observe magnetization in the direction indicated by the same arrow. The dashed circle A in Fig. 2(b) shows the spatial-frequency cutoff corresponding to the maximum resolution of the objective lens. In this configuration, due to the oblique incidence, the cutoff is contracted perpendicular to the direction of illumination, as shown by the dashed line B. This is the origin of the resolution degradation. In the high-resolution magneto-optical Kerr microscope used in this study, a set of images with different illumination directions (azimuth angles) was acquired by rotating the illumination optical path, as shown in Fig. 2(c). Since this set of images contains almost the full the spatial frequency component for the maximum resolution and the information of the vector magnetization, it is possible to reconstruct the image with full resolution and vector magnetization by appropriate arithmetic operations. The system used in this study has a spatial resolution of approximately 260 nm, using an objective lens with a numerical aperture of 0.95 (Olympus MPLAPON50×) and an illumination wavelength of 405 nm.

Pulsed-laser diodes are used as the illumination light sources in stroboscopic measurements. Compared with mode-locked lasers, which are frequently used in time-resolved measurements, semiconductor lasers are advantageous for long-time measurements owing to their stable output. However, their small output power of a few milliwatts is a disadvantage. In this study, to mitigate this problem, the outputs of two synchronously pulsed semiconductor lasers were temporally superimposed by a polarizing beam splitter to obtain twice the intensity. The lasers had a central wavelength of 405 nm, a minimum pulse width smaller than 50 ps, and a maximum repetition rate of 250 MHz. The pulse width and the repetition rate were set at 50 ps and 200 MHz, respectively.

To obtain uniform illumination, a speckle reducer consisting of a vibrating multimode fiber and microbend mode scramblers was employed. This method is suitable for illumination with a semiconductor laser because it has a smaller light loss than using a moving diffuser. Another advantage is that mechanical vibrations can be isolated from the microscope body. Because a multimode fiber was used, the elongation of the temporal pulse duration due to mode dispersion was problematic.

The bandwidth of the step-index multimode optical fiber used in this study, which had a core diameter of 200 μm and a numerical aperture of 0.39 (Thorlabs FT400EMT), was 20 MHz km at 820 nm, based on the nominal value of the manufacturer. Therefore, the bandwidth of the 2-m fiber at 405 nm was estimated as approximately 10 GHz. Although the precise pulse elongation could not be measured in our facilities, a 5.6-GHz phenomenon was observed as shown below.

Typically, in observations using magneto-optical Kerr microscopes, the angle of the analyzer is slightly tilted from the orthogonal to the polarizer. Let this angle be α and let the Kerr rotation angle of two opposite domains be $\pm\theta$. The detected optical intensities for the opposite domains are $I_\pm = I_0 \sin^2(\alpha \pm \theta)$ and, therefore, the difference in intensity is $\Delta I = I_+ - I_- = \sin(2\alpha)\sin 2\theta \approx 4\alpha\theta$. Concurrently, the contrast of the opposite domains is $2(I_+ - I_-)/(I_+ + I_-) \approx 4\alpha\theta/(\alpha^2 + \theta^2)$, which is a maximum at $\alpha = \theta$. However, the image becomes noisy because the difference in the optical intensity is small. Although increasing α improves the signal-to-noise ratio, the nonuniformity of illumination must be less than the contrast. Increasing α is desirable because the intensity of semiconductor lasers is low; however, the uniformity of illumination must be improved to achieve this. In these measurements, owing to the improved uniformity of illumination, images with good signal-to-noise ratio were obtained at $\alpha = 2$ degrees.

In high-spatial-resolution measurements, fluctuations in the room temperature can shift the focus and the sample position in a few minutes. Therefore, stabilizing them by feedback control is necessary. A monitoring system, which shares the objective lens with the observation system, was employed for this purpose. The striped patterns were projected onto the sample surface by a red light-emitting diode and the degree of focusing was detected from the monitoring images of these patterns. Shifts in the sample position were detected by the subpixel pattern-matching technique using the same monitoring images. These enabled measurements for several hours without the need for a particular laboratory environment. For reference, the capturing of the time-resolved movie with eight frames that is presented in Video 1 required approximately 100 min. The movie was obtained by acquiring a total of 131 072 images with eight microwave phases, 16 illumination directions, two analyzer angles, microwave on or off, and 256 times averaging (the latter items are the inner loops), with an exposure time of 40 ms per image.

III. SAMPLE

Figure 3(a) shows an optical image of the measured sample. The striped structures of the permalloy ($Ni_{80}Fe_{20}$), with a thickness of 40 nm, a length of 60 μm, and widths of 2, 3, 5, 7, 10, and 15 μm, were fabricated on oxidized silicon substrates using a lift-off process. Subsequently, 100-nm-thick SiO_2 was deposited for insulation and a single-wire antenna with a width of 2 μm was fabricated with Au(100 nm)/Ti(5 nm) for spin-wave excitation. An external magnetic field was applied perpendicular to the stripes. The radio-frequency (rf) current to excite the spin waves was generated by amplifying the output of a phase-locked loop synthesizer that was synchronized to a clock generator. The frequency and peak current of the rf current were 5.6 GHz and 30 mA, respectively.
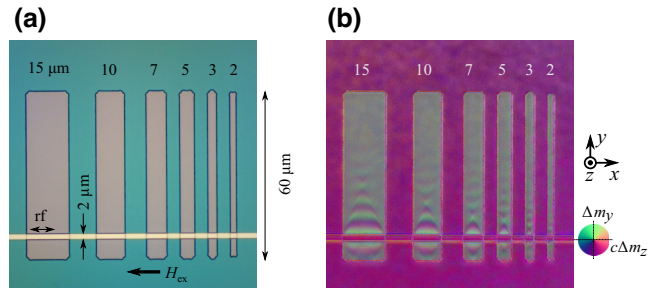

FIG. 3.   (a) An optical-microscopy image of the measured sample. (b) A typical image obtained by time-resolved magneto-optical Kerr microscopy (the movie is shown in Video 1).

IV. RESULTS AND DISCUSSION

Figure 3(b) shows a snapshot of spin waves propagating in the different stripes, under an external field of 1.7×10^4 A/m (the movie is shown in Video 1). Spin-wave propagation is noticeable at all stripe widths, showing the high spatial resolution and sensitivity of the measurement system. The pseudocolor in the images shows the direction of displacement of the magnetization vector. This represents the ability to observe vector magnetization, which is another feature of the measurement system.

In the stripes wider than 3 μm, a convergence of spin waves can be observed, which is called the self-focusing effect [2–5]. The self-focusing in a spin wave has the remarkable features that the width at the focal point is
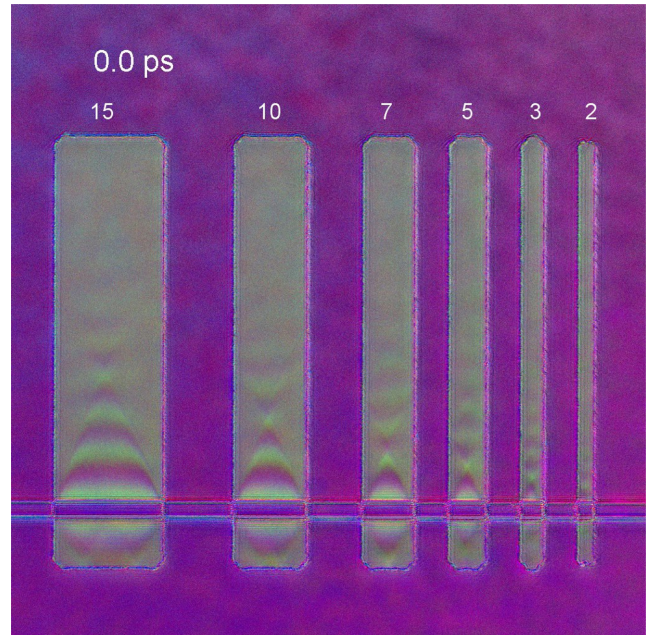
VIDEO 1.   The spin-wave propagation observed by time-resolved magneto-optical Kerr microscopy. The video consists of eight images and is repeated four times.

much smaller than half the wavelength in the propagation direction and that the beam width decreases monotonically and linearly. This is explained by the spin-wave dispersion relation as follows. Figure 4(a) shows the Fourier-transformed image of the spin-wave propagation in the 15-μm-wide stripe corresponding to the spin-wave dispersion at a frequency of 5.6 GHz [20]. The red-dashed curve is the dispersion relation obtained from the equation [20,25,26]

$$f = \frac{\mu_0 \gamma}{2\pi}$$
$$\times \sqrt{H_{ex}(H_{ex} + M_S) - H_{ex}H_d + (H_{ex} + M_S)H_d \sin^2 \phi_k}, \quad (1)$$

where f is the frequency of the spin waves, μ_0 is the vacuum permeability, γ is the gyromagnetic ratio, M_S is the saturation magnetization, ϕ_k is the angle between the external field and the propagation direction, and $H_d = M_S(1 - e^{-2|k|t})/4$, in which $|k| = \sqrt{k_x^2 + k_y^2}$. The term H_d represents the dipolar field generated by the spin waves. The first term in the square root in Eq. (1) corresponds to the frequency of the uniform ferromagnetic resonance mode (Kittel mode) and the second and third terms correspond to the frequency shift from the Kittel mode due to the spin waves. To calculate the theoretical curve, the effect of the demagnetization field was taken into account using an approximation by ellipsoids with the same aspect ratio as the stripe. The theoretical curve shows good agreement with the experiment. The approximately linear relation between k_x and k_y,

$$k_y = k_{y0} + a|k_x|, \quad (2)$$

plays an important role in the self-focusing effect. Since the amplitude of the spin wave $A(x,y)$ below the excitation antenna ($y = 0$) is constant, the amplitude of the spin wave can be expanded as

$$A(x,y) = A_0 e^{i(k_{y0}y - \omega t)} \sum_{n=0}^{\infty} \frac{(-1)^n}{2n+1}$$
$$\times \exp(i(2n+1)aky) \cos((2n+1)kx), \quad (3)$$

where $k = \pi/w$, w is the stripe width. The sum of this infinite series can be obtained analytically as

$$A(x,y) = A_0 e^{i(k_{y0}y - \omega t)} \{R(kx, aky) + iI(kx, aky)\}, \quad (4)$$

$$R(x,y) = \begin{cases} \frac{\pi}{4}, & (\cos(x+y) > 0 \text{ and } \cos(x-y) > 0), \\ -\frac{\pi}{4}, & (\cos(x+y) < 0 \text{ and } \cos(x-y) < 0), \\ 0, & (\text{otherwise}), \end{cases}$$
$$(5)$$

$$I(x,y) = \frac{1}{4} \log \left| \frac{\cos x + \sin y}{\cos x - \sin y} \right|. \quad (6)$$

Figure 4(b) shows the real part of $A(x,y)$ with $w = 15$ μm, $a = 0.36$, and $k_{y0} = 1.14$ μm^{-1}, which are estimated from Fig. 4(a). This is in good agreement with the experimental results. This can be intuitively understood as follows. At $y = 0$ in Eq. (3), each cosine component is summed with the sign of $\{+ - + - \cdots\}$, forming a step function. As there is a linear relation between k_x and k_y, this sign becomes $\{+ + + + \cdots\}$ at y, where $aky = \pi$. At this point, each cosine component is in phase at $x = 0$ and a strong peak is generated. This condition is achieved approximately due to the peculiar dispersion relation of the spin wave. The linear decrease in beam width results from a linear constant-frequency curve and the small beam width at the focal point results from its wide spread in the k_x direction. The focal length $y_{foc} = \pi/2ak = w/2a$ is proportional to the width of the stripe, which means that the angle of focusing is constant regardless of the stripe width. However, due to the effect of the demagnetization field, this relation cannot be applied directly to the experimental results. The dependence of the focal length on the stripe width is shown in Fig. 4(c). There appears to be a proportional relation between the focal length and the stripe width, as the value of a does not change significantly with the external magnetic field. The dashed blue lines show the relation $y_{foc} = w/2a$ for the stripes of 2 μm and 15 μm. In this model, the spin wave focuses periodically but the second and subsequent focusing is not clear in the experimental results. This is due to the relationship between k_x and k_y not being exactly linear and the higher-order modes decaying faster. The lack of clear self-focusing in the 2-μm-wide stripe is probably due to insufficient spatial resolution and the location of the focus point being very close to the antenna. It should be noted that the self-focusing observed in this study is essentially the same as in the previous literature [2–5] and its interpretation is also consistent with the previous work. The value of this interpretation is to point out the importance of the linear part of the dispersion relation for self-focusing. Such pronounced focusing does not occur for waves such as light waves or acoustic waves, where the relation between k_x and k_y is circular or elliptical.

The variation of the wavelength with the stripe width can also be understood using dispersion relations. The wavelengths observed in Fig. 3(b) reflect the y component of the wave number of the lowest-order propagation mode. The reciprocal of the wavelength λ is plotted versus $2/w$ in Fig. 4(d). The blue-dashed curves are constant-frequency curves for each stripe widths. The curves shift with the strip width due to the effect of the demagnetization field. The measured wavelengths are close to the corresponding constant-frequency curves, indicating that the variation in
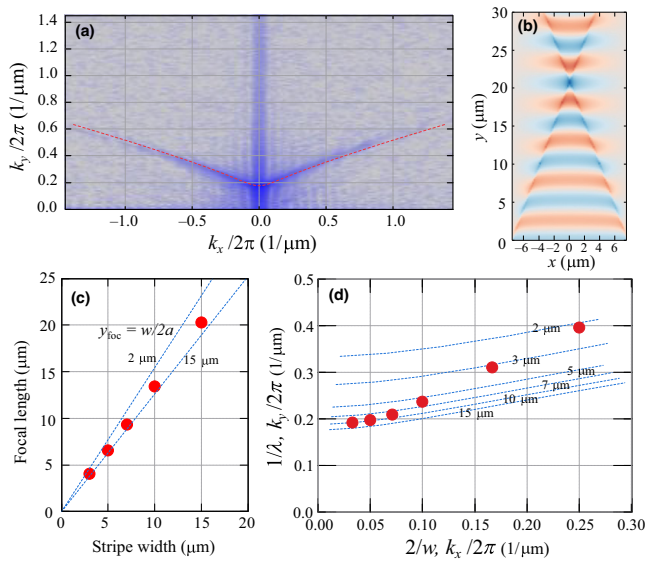
FIG. 4. (a) The Fourier-transformed image of the spin waves in the 15-μm-wide stripe. The red-dashed curve is the 5.6-GHz constant-frequency contour in the spin-wave dispersion obtained from theory. (b) An image of the spin wave reproduced by Eqs. (4)–(6). (c) The dependence of the focal length on the stripe width. The dashed blue lines show the relation $y_{\text{foc}} = w/2a$ for the stripes of 2 μm and 15 μm. (d) The relation between the wavelength λ and the stripe width w. The blue-dashed curves are constant-frequency curves for each stripe width.

FIG. 5. (a) Images of the changes in the magnetization-vector components Δm_x, Δm_y, and $c\Delta m_z$ at each time in a stripe of width 10 μm. (b) Images when the direction of the external magnetic field is reversed. $T = 1/5.6$ GHz ≈ 178.6 ps.

wavelength is well explained by the confinement effect and demagnetization.

Figure 5(a) shows the images of the vector components Δm_x, Δm_y, and $c\Delta m_z$ over one cycle of the excitation ac current in a stripe of width 10 μm. The time stamps are relative to the leftmost image. Note that the origins of Δm_y and $c\Delta m_z$ are not accurate. The magneto-optical Kerr effects are so small that nonuniform offset errors can occur for a variety of reasons. This error was removed with reference to the point where no signal was expected but this was not perfect. The in-plane magnetization components Δm_x and Δm_y are calibrated with the saturated magnetization values, whereas the out-of-plane component is not calibrated because our equipment could not saturate the magnetization in this direction. By comparison with the ratio of the amplitudes of Δm_y and Δm_z obtained by the micromagnetic simulation with the same geometry as the experiment, the constant c is estimated to be approximately 2.5. Reflection of the spin waves at the lower edge of the stripe is also observed. The amplitude of the spin waves is mainly in the y and z directions, reflecting that the equilibrium magnetization is oriented in the x direction. The phases of wave oscillation are different for Δm_y and $c\Delta m_z$, suggesting precessional motion of the magnetization.

Figure 5(b) shows the images when the direction of the external magnetic field is reversed ($H_{\text{ex}} = -1.7 \times 10^4$
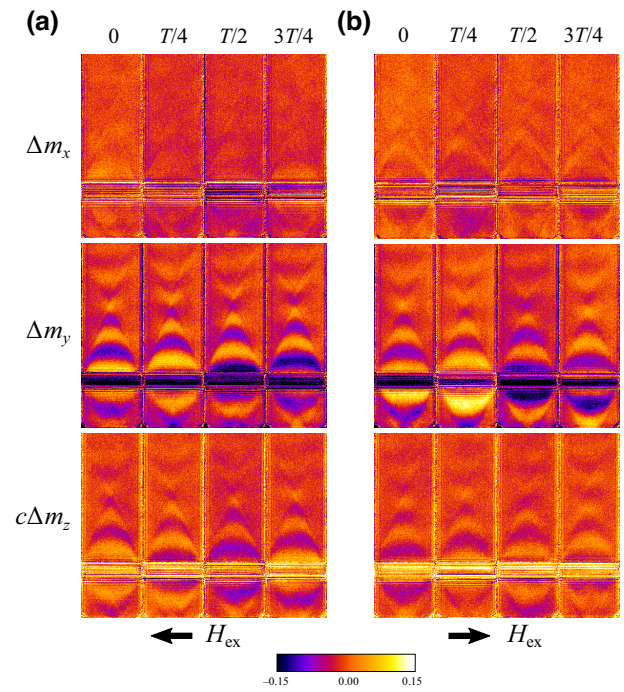
A/m) with respect to those in Fig. 5(a). The other experimental conditions are identical and, therefore, the temporal origin is common. The phase of Δm_y is almost unchanged by the reversal of the external bias field, whereas that of $c\Delta m_z$ is approximately reversed. This indicates that the direction of the precessional motion is reversed by the reversal of the bias magnetic field.

Figures 6(a) and 6(b) show the temporal behavior of Δm_y and $c\Delta m_z$ for one cycle of the excitation field. A phase shift occurs between the oscillations of Δm_y and $c\Delta m_z$, suggesting precessional motion of the magnetization. In Figs. 6(a) and 6(b), the phase of $c\Delta m_z$ is almost inverted. Figure 6(c) shows the trajectories of Δm_y and $c\Delta m_z$, indicating that the rotation direction in the y-z plane is reversed by the reversal of the external magnetic field. The spatial profiles of Δm_y and $c\Delta m_z$ are shown in Figs. 7(a) and 7(b). The sign of $c\Delta m_z$ is reversed, similar to in Figs. 6(a) and 6(b), also indicating that the direction of the precessional motion is reversed. A change as small as $\Delta m_y \sim 0.01$ is observed, showing the high sensitivity of the measurement system.

Inversion of the bias magnetic field changes the amplitude of the spin waves, which is called spin-wave nonreciprocity [27,28]. Since the excited modes are surface waves, reversal of the external magnetic field inverts the plane of propagation of the spin wave. However, in this
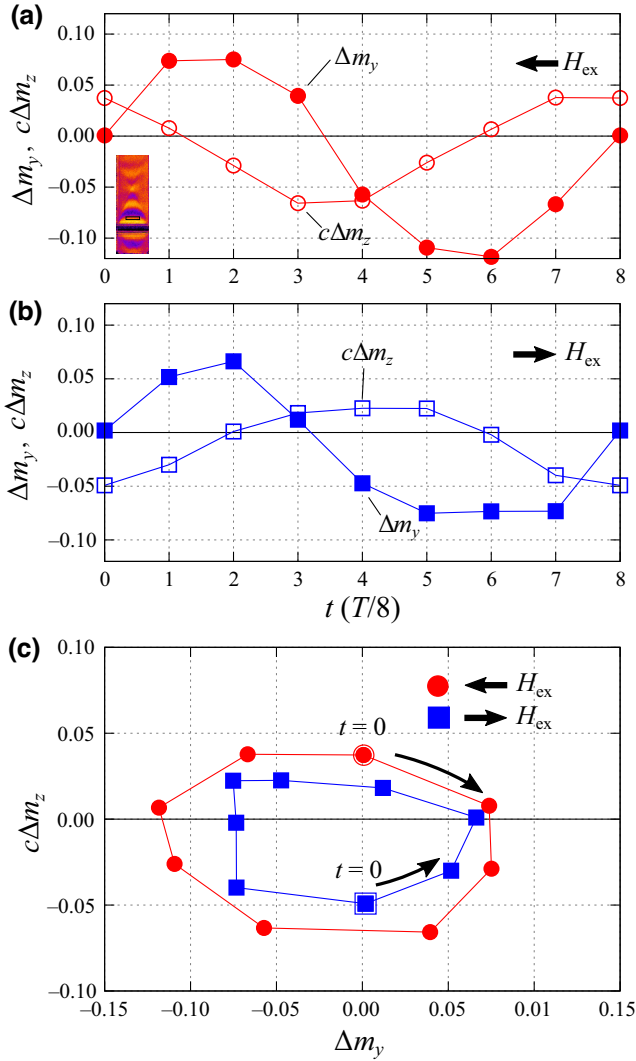
FIG. 6. (a),(b) The temporal behavior of Δm_y and $c\Delta m_z$ (a) for $H_{ex} = 1.7 \times 10^4$ A/m and (b) $H_{ex} = -1.7 \times 10^4$ A/m. The values in the boxed area in the inset are averaged. (c) Trajectories of Δm_y and $c\Delta m_z$.

FIG. 7. Spatial profiles of Δm_y and $c\Delta m_z$ for (a) $H_{ex} = 1.7 \times 10^4$ A/m and (b) $H_{ex} = -1.7 \times 10^4$ A/m. The values along the line in the inset are averaged.

component is destructive. As a result, the amplitude in Fig. 7(a) is larger than that in Fig. 7(b).

V. CONCLUSIONS

In this study, the vector-magnetization observation of spin-wave propagation was achieved by stroboscopic measurements using high-spatial-resolution magneto-optical Kerr microscopy. A characteristic self-focusing effect was clearly observed, which was explained by the peculiar dispersion relation of spin waves. Precessional motion in spin-wave propagation was also observed. The measurement system is highly sensitive and it observes spin waves with amplitudes as low as 1% saturation magnetization. This was achieved using a high-resolution magneto-optical Kerr microscope, a laser-diode light source, and a multimode fiber-based speckle reducer, and by active stabilization of the focus and the sample position. The information obtained from the measurements using this system is very rich and intuitive. It is anticipated that the developed measurement technique will prove to be a powerful method in studying spin waves and spintronics.

case, the thickness of the sample is much less than the characteristic depth of the surface wave; therefore, this is not a sufficient explanation for the observed difference in amplitude. This is intuitively understood by the relation between the direction of the precession and the spatial distribution of the excitation field. Since the excitation antenna is placed above the strip, the z component of the excitation field H_z is positive in $y > 0$ and negative in $y < 0$ if H_y is positive at $y = 0$, and vice versa. In Fig. 7(a), since Δm_y is positive at $y = 0$ and $c\Delta m_z$ is also positive at around $y \sim 2$ μm, the excitation by the z component of the field is constructive to this mode. On the other hand, when the external field is inverted, as seen in Fig. 7(b), the sign of the $c\Delta m_z$ is negative; therefore, the excitation by the z
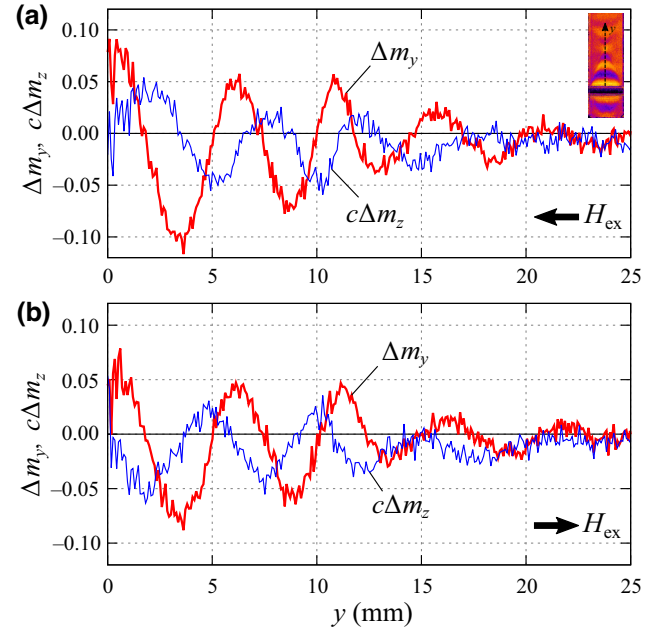
[1] A. V. Chumak, V. Vasyuchka, A. Serga, and B. Hillebrands, Magnon spintronics, Nat. Phys. **11,** 453 (2015).

[2] M. Bauer, O. Büttner, S. O. Demokritov, B. Hillebrands, V. Grimalsky, Y. Rapoport, and A. N. Slavin, Observation of Spatiotemporal Self-Focusing of Spin Waves in Magnetic Films, Phys. Rev. Lett. **81,** 3769 (1998).

[3] O. Büttner, M. Bauer, S. O. Demokritov, B. Hillebrands, Y. S. Kivshar, V. Grimalsky, Y. Rapoport, M. P. Kostylev, B. A. Kalinikos, and A. N. Slavin, Spatial and spatiotemporal self-focusing of spin waves in garnet films observed by space- and time-resolved Brillouin light scattering, J. Appl. Phys. **87,** 5088 (2000).

[4] V. E. Demidov, S. O. Demokritov, K. Rott, P. Krzysteczko, and G. Reiss, Self-focusing of spin waves in Permalloy microstripes, Appl. Phys. Lett. **91,** 252504 (2007).

[5] V. E. Demidov, S. O. Demokritov, K. Rott, P. Krzysteczko, and G. Reiss, Mode interference and periodic self-focusing of spin waves in permalloy microstripes, Phys. Rev. B **77,** 064406 (2008).

[6] V. E. Demidov and S. O. Demokritov, Magnonic waveguides studied by microfocus Brillouin light scattering, IEEE Trans. Magn. **51,** 0800215 (2015).

[7] M. Madami, G. Gubbiotti, S. Tacchi, and G. Carlotti, Application of microfocused Brillouin light scattering to the study of spin waves in low-dimensional magnetic systems (2012). doi:10.1016/B978-0-12-397028-2.00002-3

[8] T. Sebastian, K. Schultheiss, B. Obry, B. Hillebrands, and H. Schultheiss, Micro-focused Brillouin light scattering: Imaging spin waves at the nanoscale, Front. Phys. **3,** 35 (2015).

[9] F. Groß, N. Träger, J. Förster, M. Weigand, G. Schütz, and J. Gräfe, Nanoscale detection of spin wave deflection angles in permalloy, Appl. Phys. Lett. **114,** 012406 (2019).

[10] J. Gräfe, P. Gruszecki, M. Zelent, M. Decker, K. Keskinbora, M. Noske, P. Gawronski, H. Stoll, M. Weigand, M. Krawczyk, C. H. Back, E. J. Goering, and G. Schütz, Direct observation of spinwave focusing by a Fresnel lens, Phys. Rev. B **102,** 024420 (2020).

[11] N. Träger, P. Gruszecki, F. Lisiecki, F. Groß, J. Förster, M. Weigand, H. Głowiński, P. Kuświk, J. Dubowik, G. Schütz, M. Krawczyk, and J. Gräfe, Real-Space Observation of Magnon Interaction with Driven Space-Time Crystals, Phys. Rev. Lett. **126,** 057201 (2021).

[12] S. Tamaru, J. A. Bain, R. J. M. van de Veerdonk, T. M. Crawford, M. Covington, and M. H. Kryder, Imaging of quantized magnetostatic modes using spatially resolved ferromagnetic resonance, J. Appl. Phys. **91,** 8034 (2002).

[13] S. Tamaru, J. A. Bain, R. J. M. van de Veerdonk, T. M. Crawford, M. Covington, and M. H. Kryder, Measurement of magnetostatic mode excitation and relaxation in permalloy films using scanning Kerr imaging, Phys. Rev. B **70,** 104416 (2004).

[14] S. Mansfeld, J. Topp, K. Martens, J. N. Toedt, W. Hansen, D. Heitmann, and S. Mendach, Spin Wave Diffraction and Perfect Imaging of a Grating, Phys. Rev. Lett. **108,** 047204 (2012).

[15] J. Stigloher, M. Decker, H. S. Körner, K. Tanabe, T. Moriyama, T. Taniguchi, H. Hata, M. Madami, G. Gubbiotti, K. Kobayashi, T. Ono, and C. H. Back, Snell's Law for Spin Waves, Phys. Rev. Lett. **117,** 037204 (2016).

[16] J.-N. Toedt, M. Mundkowski, D. Heitmann, S. Mendach, and W. Hansen, Design and construction of a spin-wave lens, Sci. Rep. **6,** 33169 (2016).

[17] P. Wessels, A. Vogel, J. N. Tödt, M. Wieland, G. Meier, and M. Drescher, Direct observation of isolated Damon-Eshbach and backward volume spin-wave packets in ferromagnetic microstripes, Sci. Rep. **6,** 22117 (2016).

[18] R. B. Holländer, C. Müller, M. Lohmann, B. Mozooni, and J. McCord, Component selection in time-resolved magneto-optical wide-field imaging for the investigation of magnetic microstructures, J. Magn. Magn. Mater. **432,** 283 (2017).

[19] H. S. Körner, J. Stigloher, and C. H. Back, Excitation and tailoring of diffractive spin-wave beams in NiFe using nonuniform microwave antennas, Phys. Rev. B **96,** 100401(R) (2017).

[20] Y. Shiota, S. Funada, R. Hisatomi, T. Moriyama, and T. Ono, Imaging of caustic-like spin wave beams using optical heterodyne detection, Appl. Phys. Lett. **116,** 192411 (2020).

[21] W. Rave, R. Schäfer, and A. Hubert, Quantitative observation of magnetic domains with the magneto-optical Kerr effect, J. Magn. Magn. Mater. **65,** 7 (1987).

[22] T. V. Hofe, N. O. Urs, B. Mozooni, T. Jansen, C. Kirchhof, D. E. Bürgler, E. Quandt, and J. McCord, Dual wavelength magneto-optical imaging of magnetic thin films, Appl. Phys. Lett. **103,** 142410 (2013).

[23] T. Ogasawara, Improvement in spatial frequency characteristics of magneto-optical Kerr microscopy, Jpn. J. Appl. Phys. **56,** 108002 (2017).

[24] T. Ogasawara and A. Yamaguchi, Observation of frequency dependent resonances in magnetic vortex core gyration using time-resolved magneto-optical Kerr microscope with pulsed semiconductor laser illumination, Jpn. J. Appl. Phys. **61,** 018001 (2022).

[25] R. Damon and J. Eshbach, Magnetostatic modes of a ferromagnet slab, J. Phys. Chem. Solids **19,** 308 (1961).

[26] B. A. Kalinikos and A. N. Slavin, Theory of dipole-exchange spin wave spectrum for ferromagnetic films with mixed exchange boundary conditions, J. Phys. C: Solid State Phys. **19,** 7013 (1986).

[27] K. Sekiguchi, K. Yamada, S. M. Seo, K. J. Lee, D. Chiba, K. Kobayashi, and T. Ono, Nonreciprocal emission of spin-wave packet in FeNi film, Appl. Phys. Lett. **97,** 022508 (2010).

[28] M. Nakayama, K. Yamanoi, S. Kasai, S. Mitani, and T. Manago, Thickness dependence of spin wave nonreciprocity in permalloy film, Jpn. J. Appl. Phys. **54,** 083002 (2015).